Fibro-Adipogenic Remodeling of the Diaphragm in Obesity-Associated Respiratory Dysfunction

Eric D. Buras,[1,2] Kimber Converso-Baran,[3] Carol S. Davis,[3] Takeshi Akama,[1,2] Fumihito Hikage,[1,2] Daniel E. Michele,[3] Susan V. Brooks,[3,4] and Tae-Hwa Chun[1,2]

Diabetes 2019;68:45–56 | https://doi.org/10.2337/db18-0209

Respiratory dysfunction is a common complication of obesity, conferring cardiovascular morbidity and increased mortality and often necessitating mechanical ventilatory support. While impaired lung expansion in the setting of increased adipose mass and reduced central response to hypercapnia have been implicated as pathophysiological drivers, the impact of obesity on respiratory muscles—in particular, the diaphragm—has not been investigated in detail. Here, we demonstrate that chronic high-fat diet (HFD) feeding impairs diaphragm muscle function, as assessed in vivo by ultrasonography and ex vivo by measurement of contractile force. During an HFD time course, progressive adipose tissue expansion and collagen deposition within the diaphragm parallel contractile deficits. Moreover, intradiaphragmatic fibro-adipogenic progenitors (FAPs) proliferate with long-term HFD feeding while giving rise to adipocytes and type I collagen–depositing fibroblasts. Thrombospondin 1 (THBS1), a circulating adipokine, increases with obesity and induces FAP proliferation. These findings suggest a novel role for FAP-mediated fibro-adipogenic diaphragm remodeling in obesity-associated respiratory dysfunction.

Obesity-associated respiratory complications range from simple dyspnea on exertion to life-threatening obesity hypoventilation syndrome (OHS) (1). OHS—defined by $PaCO_2$ >45 mmHg in individuals with BMI ≥30 kg/m^2 and no alternative cause of hypercapnia—impacts 2 million Americans (2) and exacerbates risks of heart failure and early mortality (3).

OHS pathophysiology is incompletely understood; however, restricted lung expansion in the setting of excess thoracic and visceral adipose tissue is assumed to be a major driver (4). Clinical studies demonstrate respiratory muscle weakness parallels this physical restriction (5,6), while autopsy samples from OHS patients contain prominent intradiaphragmatic adipocyte inclusions (7). These findings suggest that anatomic remodeling of the diaphragm itself may contribute to obesity-induced respiratory impairment.

Preclinical studies of respiratory function in obesity have largely employed genetically obese Zucker diabetic fatty (*ZDF*) rats. In this model, ex vivo diaphragmatic testing has yielded equivocal results, with contractile force reduced in older animals (8) but unchanged (9,10) or increased (11) in younger animals. *ob/ob* mice demonstrate hypoventilation reversible by leptin infusion, indicating that this adipokine may regulate central respiratory drive (12). Nonetheless, ventilatory function in diet-induced obese (DIO) models is unaffected by this maneuver (12), suggesting that exploration of other mechanisms, including intrinsic diaphragm compromise, is warranted to better understand the pathogenesis of obesity-induced respiratory dysfunction.

Accumulation of intramuscular adipose tissue (IMAT) is a complication of immobility (13) and muscular dystrophy (14). IMAT increases with normal aging (15) and quantitatively correlates with reduced muscle strength in the elderly (16). Recent studies demonstrate that IMAT expansion is also associated with weakness in individuals with obesity and type 2 diabetes (17–19).

[1]Division of Metabolism Endocrinology and Diabetes, Department of Internal Medicine, University of Michigan, Ann Arbor, MI
[2]Biointerfaces Institute, University of Michigan, Ann Arbor, MI
[3]Department of Molecular and Integrative Physiology, University of Michigan, Ann Arbor, MI
[4]Department of Biomedical Engineering, University of Michigan, Ann Arbor, MI
Corresponding author: Tae-Hwa Chun, taehwa@med.umich.edu

Received 19 February 2018 and accepted 3 October 2018

This article contains Supplementary Data online at http://diabetes.diabetesjournals.org/lookup/suppl/doi:10.2337/db18-0209/-/DC1.

See accompanying article, p. 18.

Intramuscular fibrosis accompanies impaired regeneration, increased tissue stiffness, and reduced contractile force in skeletal muscle disorders (20). Intramuscular extracellular matrix (ECM) deposition is associated with insulin resistance in obese mice (21–23), while upregulation of skeletal muscle collagen gene expression occurs in humans after lipid infusion (24) and experimental overfeeding (25) and with chronic obesity (26). Despite links between overnutrition and ECM remodeling, direct effects of these fibrotic changes on muscle contraction remain largely undefined. Thrombospondin 1 (THBS1), a circulating ECM protein, activates transforming growth factor β (TGF-β) (27), promotes mesenchymal cell proliferation (28), and underlies fibrosis in limb muscles of obese mice (21).

Fibro-adipogenic progenitors (FAPs) are mesenchymal cells residing within skeletal muscle that give rise to adipocytes and fibroblasts in mice and humans (29–31). Largely quiescent at baseline, FAPs proliferate in response to muscle injury, facilitating muscle regeneration (32,33). In the *mdx* mouse model of muscular dystrophy, disordered FAP dynamics contribute to pathological adiposity and fibrosis (34,35). While FAPs may remodel skeletal muscle in obesity, their response to metabolic challenge remains unexamined. In this study, we tested whether fibro-adipogenic diaphragm remodeling occurs in obesity-associated respiratory impairment and whether FAPs contribute to the process.

RESEARCH DESIGN AND METHODS

Animals

Mice were obtained from The Jackson Laboratory (Bar Harbor, ME). The Jackson Laboratory maintains *Sca-1 GFP* (cat. no. 12643), *PDGFRα-Cre* (013148), and *ob/ob* (000632) mice on a *C57BL/6J* background and *mT/mG* (007576) mice on a *129X1/SvJ* background. Animals were maintained in pathogen-free housing with a 12-h light-dark cycle and ad libitum food and water. For DIO studies, mice received a normal chow diet (CD) (5L0D; LabDiet, St Louis, MO) until 8 weeks of age. Control mice continued CD, while experimental mice switched to a high-fat diet (HFD) containing 45% calories from lipid (D12451; Research Diets, New Brunswick, NJ). Mice consumed the CD or HFD for 1, 3, or 6 months before analyses. For comparisons of *ob/ob* and wild-type (WT) *C57BL/6J* mice, all animals consumed CD and were analyzed at 16 weeks of age. The University of Michigan Institutional Animal Care and Use Committee approved all studies.

Diaphragm Ultrasonography

As previously described (36), diaphragms were localized by ultrasound (US) using a transversely oriented MS250 transducer (frequency 24 MHz) (Vevo 2100; Visual Sonics, Toronto, ON). Diaphragm motion, observed in M-mode, was recorded for three or more respiratory cycles. Excursion amplitude, inspiratory duration, inspiratory velocity, expiratory velocity, and peak-to-peak time were measured on still images. Inspiratory duty cycle was calculated as the quotient of inspiratory duration/peak-to-peak time.

Ex Vivo Isometric Testing

Twitch properties and tetanic force (37) were measured on 2- to 4-mm-wide lateral costal diaphragm strips. In a Krebs-Ringer bath containing 0.03 mmol/L tubocurarine chloride, held at 25°C and bubbled with 95% O_2 and 5% CO_2 (maintaining pH 7.4), an attached rib was sutured to a servomotor (model 305B; Aurora Scientific, Aurora, ON) and the free central tendon edge to a force transducer (model BG-50; Kulite Semiconductor Products, Leonia, NJ). The bath was electrically stimulated through a field generated between two platinum electrodes by a biphasic current stimulator (model 701A; Aurora Scientific). LabVIEW 2014 software (National Instruments, Austin, TX) controlled electrical pulse properties and servomotor activity while recording transducer data. Strips were adjusted to optimal length (L_o) at which a stimulus pulse elicited maximum isometric force (P_o). Resting tension was measured at L_o. Contraction and half-relaxation times were measured during individual isometric twitches. Muscle cross-sectional area (CSA) was calculated using L_o and muscle mass. Specific force was calculated as the quotient of P_o/CSA.

Stromal Cell Analysis

Diaphragmatic stromal cells were isolated through a protocol adapted from one previously described (30). Costal diaphragms were excised, minced, and digested in collagenase type II (Worthington Biochemical, Lakewood, NJ) diluted to 0.067% by weight in serum-free DMEM (Thermo Fisher Scientific, Waltham, MA). After 1 h at 37°C, collagenase was inactivated with DMEM containing 10% FBS. Resultant suspensions were sequentially passed through 100-μm and 40-μm cell strainers.

Flow cytometry used established marker profiles (29). Briefly, cells isolated from *Sca-1 GFP* mice were fixed with 4% paraformaldehyde (PFA), permeabilized/blocked in 0.3% Triton X-100 with 5% normal goat serum, and then incubated with fluorophore-conjugated CD31, CD45, integrin α7, and platelet-derived growth factor receptor α (PDGFRα) antibodies (Supplementary Table 1). After DAPI staining, cells were analyzed on a MoFlo Astrios EQ running Summit software (version 6.3; Beckman-Coulter, Brea, CA). Gates were established using fluorescence minus one for labeled antibodies and WT littermate for (Sca-1) GFP. Cell cycle analysis was performed based on nuclear DAPI staining. For gene expression and ex vivo analyses of stromal isolates from WT mice, cells were purified by two-step magnetic-assisted cell sorting employing MiniMACS columns (Miltenyi, Bergisch Gladbach, Germany) following the manufacturer's instructions. Cells were first subjected to negative selection using Lin (CD31 and CD45) antibodies (130-09-858). Resulting Lin^- cells were sequentially incubated with FITC-conjugated Sca-1 antibody (120-003-751) and anti-FITC microbeads (120-003-754). $Lin^-/Sca\text{-}1^+$ (FAP), and $Lin^-/Sca\text{-}1^-$ (non-FAP)-enriched populations were subsequently analyzed.

Gene Expression Analysis

Whole tissues—costal diaphragm and brown adipose tissue (BAT)—were cleaned of adherent tissues, snap frozen, and digested in Trizol (Thermo Fisher) with mechanical homogenization, while stromal cells subjected to magnetic-assisted cell sorting (MACS) isolation were pelleted by centrifugation. Both underwent RNEasy-based RNA isolation following the manufacturer's instructions (Qiagen, Germantown, MD). cDNA synthesis with SuperScript II (Invitrogen, Carlsbad, CA) preceded quantitative PCR with SYBR Green (Thermo Fisher Scientific) or Taqman (Applied Biosystems, Foster City, CA) on a StepOnePlus machine (Applied Biosystems). Primer/probe sequences are indicated in Supplementary Table 2.

Cell Culture

After isolation, stromal cells were cultured for 1 day in 24-well plates containing standard medium: DMEM with 10% FBS and antibiotic/antimycotic (penicillin, streptomycin, and amphotericin B; Sigma-Aldrich, St Louis, MO). Cells were then seeded at 30% confluence in four-well chamber slides (Lab Tek; Thermo Fisher Scientific) with standard medium. Those allocated for Ki67 and extracellular collagen staining were evaluated after 3 days. Those allocated for adipogenesis were cultured for 5 days (reaching full confluence), then switched to standard medium plus adipogenic cocktail (1 μg/mL insulin, 250 nmol/L dexamethasone, 10 μmol/L troglitazone, and 10 nmol/L triiodothyronine) for 7 days, and then switched to standard medium plus insulin (1 μg/mL) for 3 days. After each experiment, cells were fixed, blocked, and immunostained as previously described (38). For Ki67 staining, wash buffers and antibody diluents contained 0.2% Tween-20. This was excluded for extracellular collagen staining. Cells subjected to adipogenesis analysis were fixed and then incubated in BODIPY-543 (Thermo Fisher Scientific). Cells subjected to THBS1 treatment were transferred to slide wells containing standard medium for 12 h and then switched to DMEM with 1% FBS. Subsequently, individual groups were incubated in this medium with or without THBS1 (cat. no. 605225; Calbiochem, San Diego, CA) at 0, 1, or 5 μg/mL, followed by Ki67 staining. Counterstain with Alexa Fluor 488–conjugated phalloidin (Thermo Fisher Scientific) was used in specific experiments.

Decellularization/Oil Red O Staining

As previously described (39), whole diaphragms were decellularized in 1% SDS for 5 days, fixed in 4% PFA, and then incubated in Oil red O (ORO) dissolved to 0.3% by weight in 60% isopropanol. After overnight incubation in 1% SDS, they were affixed to wax plates or dissection petri dishes for analysis.

Histological Analysis

Six-μm-thick formalin-fixed, paraffin-embedded sections of costal hemidiaphragm, BAT, and inguinal and gonadal white adipose tissue (WAT) were prepared as previously described (21) and stained with Sirius red, hematoxylin-eosin (H-E), and Masson trichrome by standard procedures. Immunohistochemistry on formalin-fixed, paraffin-embedded sections was performed as described in (21), with primary and secondary antibodies indicated in (Supplementary Table 1). Full-thickness diaphragm chunks (4 mm^2) fixed in 1% PFA for 5 min at room temperature were used for immunofluorescent detection of type I and VI collagen by whole-mount confocal microscopy. All processing was performed in detergent-free solutions. Samples were imaged using an Olympus DP72 camera mounted on an Olympus SZ61 microscope (Tokyo, Japan) or a Nikon A1 confocal microscope running NIS-Elements software (Olympus). Three nonconsecutive sections per animal were used for quantitative morphometry, with analysis performed using NIH ImageJ.

Western Blot

Plasma (1 μL) was diluted in SDS lysis buffer, denatured, and run in 5% SDS-PAGE. THBS1 was detected by Western blot using rabbit anti-THBS1 antibody (Santa Cruz Biotechnology, Santa Cruz, CA) as previously described (21).

Statistical Analysis

Data analysis employed Student *t* test for two-group comparisons, one-way ANOVA (with Tukey post hoc test) comparisons of two or more groups, two-way ANOVA (with Sidak post hoc test) for two variables, and linear regression for correlation analysis. *P* value <0.05 indicated statistical significance. Data are shown as mean ± SD.

RESULTS

Diaphragm Motion Compromise With Long-term HFD Challenge

To generate a model of obesity-induced respiratory dysfunction, we placed male *C57BL/6J* mice on a 6-month DIO time course, observing marked weight gain (Fig. 1*A*) and glucose intolerance (Supplementary Fig. 1*A*) in HFD-fed animals versus CD-fed counterparts. We analyzed diaphragm motion with noninvasive US (Fig. 1*B*). This technique is validated in rodents, and US-based measurement of diaphragm excursion amplitude correlates with ex vivo isometric force values in WT and *mdx* mice (36). In our animals, amplitude was unchanged between groups at 3 months but significantly lower in HFD-fed animals after 6 months (Fig. 1*C*). Similar HFD-induced declines occurred in inspiratory and expiratory velocity (Fig. 1*D* and *E*). Additionally, 6-month HFD mice displayed increased respiratory rates, indicated by reduced peak-to-peak time (Fig. 1*F*). Duty cycle, denoting percentage of each breath spent in inspiration (inspiratory duration/peak-to-peak time), also increased significantly with 6-month HFD feeding (Fig. 1*G*). These data indicate that long-term DIO impairs diaphragm motion, inducing restrained, low-amplitude contractions occurring at shorter intervals.

We analyzed diaphragm motion in *ob/ob* mice, which, at 16 weeks of age, had weights comparable with those of

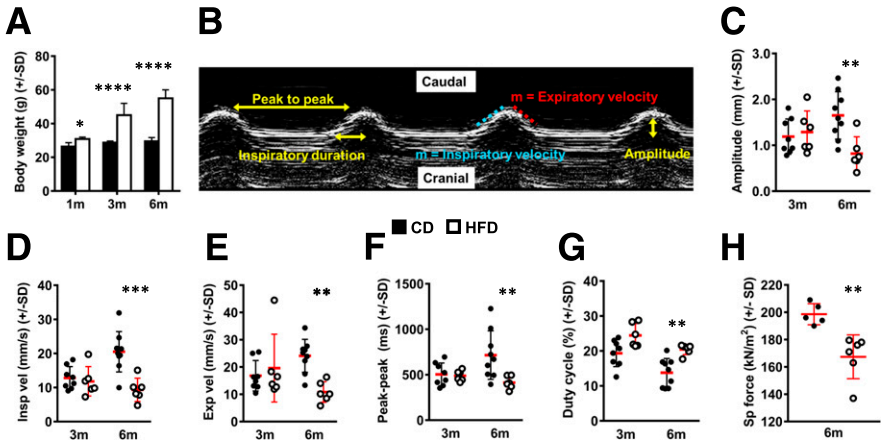

Figure 1—Long-term DIO impairs diaphragm function. *A*: Total body weight (g) of CD- and HFD-fed mice after 1 month (1m), 3 months (3m), and 6 months (6m) of feeding. *B*: M-mode US tracing of diaphragmatic motion with measured parameters labeled. *C*: Amplitude (mm). *D*: Inspiratory velocity (Insp vel) (mm/s). *E*: Expiratory velocity (Exp vel) (mm/s). *F*: Peak-to-peak time (ms). *G*: Duty cycle (inspiratory duration/peak to peak) (percent). *H*: Specific (Sp) force (kN/m^2) measured on 2- to 4-mm-wide costal diaphragm strips isolated from CD- and HFD-fed mice at the 6-month time point. Each point represents mean value of measurements taken from two strips per animal. n = 7 CD and 4 HFD mice at 1-month time point, 8 CD and 6 HFD mice at 3-month time point, and 5–9 CD and 6 HFD mice at 6-month time point. Data analysis employed Student t test for two-group, single-variable comparisons and two-way ANOVA (with Sidak post hoc test) for two-variable comparisons. $^*P < 0.05$; $^{**}P < 0.01$; $^{***}P < 0.001$; $^{****}P < 0.0001$.

6-month DIO animals (Supplementary Fig. 2*A*). When compared with age-matched WT controls, *ob/ob* mice also showed reduced amplitude (Supplementary Fig. 2*B*), inspiratory velocity (Supplementary Fig. 2*C*), expiratory velocity (Supplementary Fig. 2*D*), and peak-to-peak time (Supplementary Fig. 2*E*); however, duty cycle was unchanged (Supplementary Fig. 2*F*). As such, *ob/ob* animals displayed similar, but not identical, diaphragm motion defects versus DIO mice.

Intrinsic Diaphragm Contractile Compromise in Long-term DIO

We next tested whether observed ultrasonographic changes resulted from functional defects intrinsic to the diaphragm. We specifically evaluated its costal region (40) (Supplementary Fig. 1*B*), previously shown to be responsible for contractile force generation (41), by performing ex vivo isometric testing (Supplementary Fig. 1*C*). Indeed, specific force, defined as maximum tetanic force per unit CSA, was >15% lower in 6-month HFD versus CD mice (Fig. 1*H*). Specific force measurements from individual animals correlated with excursion amplitudes (Supplementary Fig. 1*D*) and exhibited negative linear relationships with body weight (Supplementary Fig. 1*E*) and inguinal adipose mass (Supplementary Fig. 1*F*). Resting tension, time to peak tetanus, and half-relaxation time were unchanged with HFD feeding (Supplementary Fig. 1*G–I*). Notably, the reduced force generation induced by HFD feeding was not associated with significant changes in costal diaphragm thickness, average myofiber diameter, or percentage of muscle CSA occupied by myofibers (Supplementary Fig. 1*J–M*). In contrast with DIO mice, specific force measurements from *ob/ob* diaphragms were nearly identical to those of controls (Supplementary Fig. 2*G*). This result parallels prior reports of normal diaphragm contractile force in young *ZDF* rats (9,10) and is consistent with findings that *ob/ob* hypoventilation can be quickly reversed by leptin infusion (12).

DIO Induces Progressive Intradiaphragmatic Adiposity

Since long-term DIO yielded intrinsic diaphragmatic contractile compromise without obvious differences in myofiber morphology, we assessed whether other anatomic changes accompanied physiological impairment. First, we analyzed adiposity using decellularized diaphragms of 6-month CD and HFD mice. In CD-fed animals, ORO staining revealed well-demarcated lipid droplets closely juxtaposed with apparent branches of the phrenic vasculature (40) (Fig. 2*A* and *B*). HFD feeding increased ORO-positive droplet number and size, especially in the lateral costal diaphragm (Fig. 2*A* and *B*). H-E staining of costal diaphragm sections also showed unilocular adipocytes (Fig. 2*C*), with their identity confirmed by perilipin immunohistochemistry (Fig. 2*D*). These localized near blood vessels in CD-fed mice but extended farther into the tissue with HFD feeding (Fig. 2*C*). CSA of individual adipocytes increased after 1 month of HFD feeding (Fig. 2*E*) and was threefold greater versus that in controls at 3 and 6 months (Fig. 2*E*). Size distribution profiling demonstrated adipocytes in CD diaphragms to be small: CSA ≤250 μm^2 for the majority (Fig. 2*F*). On the contrary, in HFD diaphragms many adipocytes displayed CSA ≥1,000 μm^2 (Fig. 2*F*). Adipocyte number was statistically unchanged between groups at 1 and 3 months but was significantly elevated with HFD feeding at 6 months (Fig. 2*G*). Percentage of diaphragm CSA occupied by adipocytes also increased significantly with HFD feeding only at the 6-month

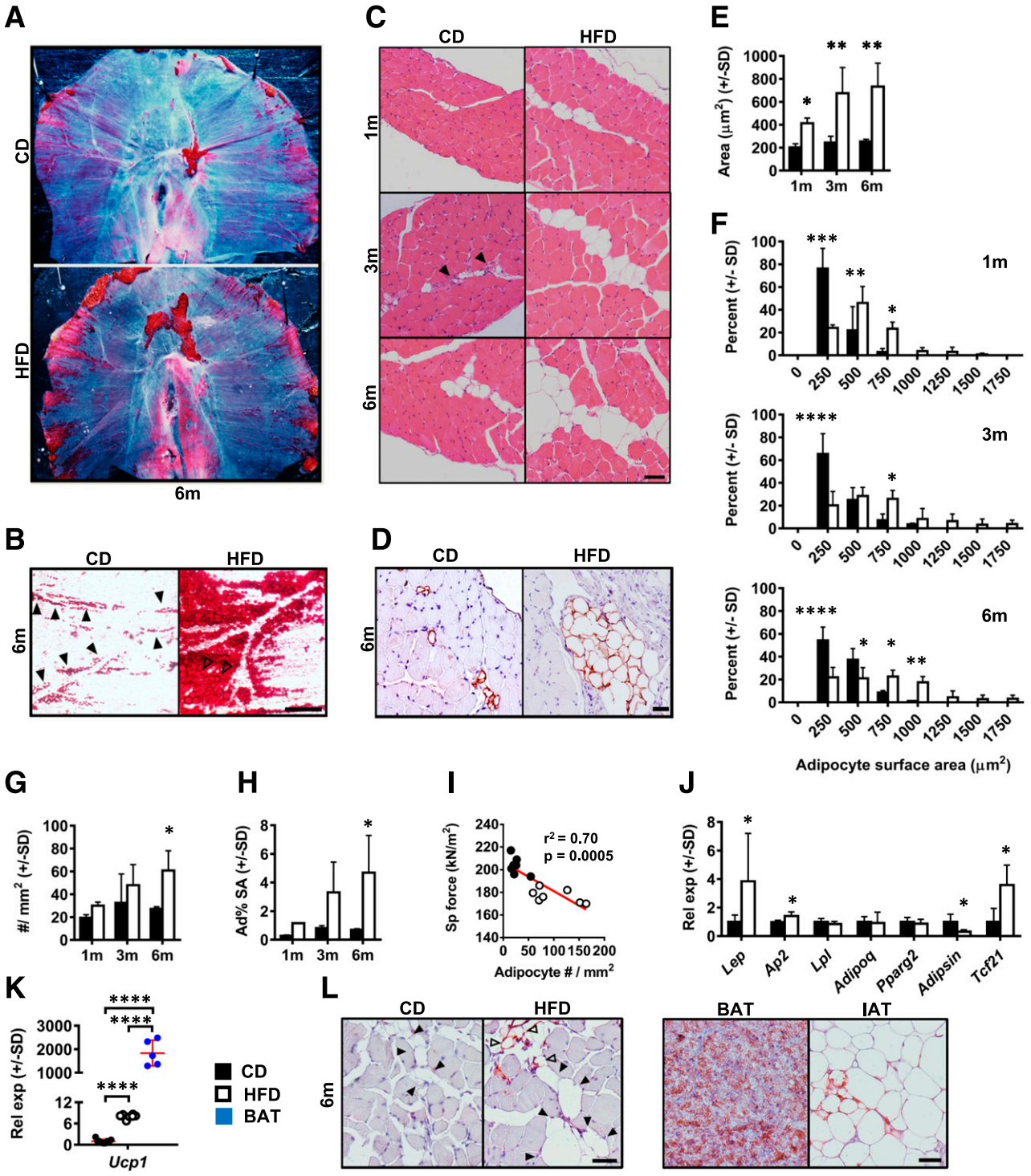

Figure 2—DIO causes progressive intradiaphragmatic adiposity. *A*: Decellularized whole diaphragms, stained with ORO, from 6-month (6m) CD and HFD mice. Representative images from 4 animals per group. *B*: Decellularized diaphragm (from same groups) demonstrating lateral costal region under transillumination. Filled arrowheads (in CD sample) indicate adipocyte distribution near putative phrenic vasculature. Open arrowheads (in HFD) show a conglomeration of large lipid droplets. Scale bar = 400 μm. *C*: H-E sagittal sections of CD and HFD costal diaphragms at 1-month (1m), 3-month (3m), and 6-month time points. Closed arrowheads (in CD sample) indicate blood vessels (frequently seen in close opposition to adipocytes). Representative images from four to six animals per group. Scale bar = 25 μm. *D*: Perilipin-stained sagittal costal diaphragm sections from 6-month CD and HFD mice. Representative images from four animals per group. Scale bar = 25 μm. *E*: Average cross-sectional surface area of individual costal diaphragm adipocytes (μm^2) in CD- and HFD-fed mice at 1-month, 3-month, and 6-month time points. $n = 4$ mice per group at each time point. *F*: Costal diaphragm individual adipocyte cross-sectional surface area shown as frequency distribution for 1-month, 3-month, and 6-month CD and HFD mice. $n = 4$ mice per group at each time point. *G*: Number of costal diaphragm adipocytes per mm^2 muscle cross-sectional tissue surface area at 1-month, 3-month, and 6-month time points. $n = 4$ mice per group at each time point. *H*: Percentage costal diaphragm cross-sectional surface area occupied by adipocytes (Ad% SA) at 1-month, 3-month, and 6-month time points. $n = 4$ mice per group at each time point. *I*: Correlation plot showing relationship between adipocyte

time point (Fig. 2*H*). Notably, intradiaphragmatic adipocyte number negatively correlated with specific force in individually assessed diaphragm strips (Fig. 2*I*).

Transcripts encoding mature adipocyte markers fatty acid binding protein (FABP4) and leptin, as well as a WAT marker, TCF21 (42), increased with HFD feeding. On the contrary, those encoding lipoprotein lipase (LPL), adiponectin, and PPARγ were unchanged. As seen in other adipose depots (43), diaphragmatic *adipsin* declined with DIO (Fig. 2*J*). WAT exhibits obesity-induced inflammation and macrophage infiltration (44). While DIO diaphragms showed no change in *Il1b*, *Tnfa*, and *Il6* (Supplementary Fig. 3*A*), *Emr1*, encoding macrophage marker F4/80, increased marginally with HFD feeding (Supplementary Fig. 3*A*). Nonetheless, we observed few F4/80$^+$ cells and no discernable crown-like structures in diaphragms of CD- or HFD-fed mice (Supplementary Fig. 3*B*). Interestingly, DIO diaphragms showed strong *Ucp1* induction, albeit at a low level versus BAT (Fig. 1*K*). Consistent with this, immunohistochemistry revealed isolated UCP1$^+$ unilocular adipocytes among many UCP1$^-$ cells (Fig. 1*L*). Together, these findings suggest that intradiaphragmatic IMAT exhibits WAT-like characteristics and ability to express UCP1 after metabolic challenge (45).

Notably, diaphragms of *ob/ob* mice, which demonstrated no ex vivo contractile defects, had larger adipocytes (Supplementary Fig. 2*H* and *I*) but equivalent adipocyte number relative to those of WT controls (Supplementary Fig. 2*J*).

Progressive Diaphragm Fibrosis in DIO

Given association of intramuscular ECM deposition with obesity (21–26) and contractile dysfunction (20), we postulated that DIO diaphragms might undergo fibrotic remodeling. Indeed, percentage of costal diaphragm CSA occupied by polymerized collagen progressively increased during HFD feeding (Fig. 3*A*), becoming statistically elevated versus controls by 6 months (Fig. 3*B*). With DIO, collagen deposition was especially apparent near adipocytes (Fig. 3*C*). Moreover, within strips subjected to isometric testing, polymerized collagen area negatively correlated with specific force measurements (Fig. 3*D*).

Gene expression analysis of 6-month costal diaphragms revealed HFD-induced increases in transcripts encoding type I and VI collagen (Fig. 3*E*). On the contrary, levels of those encoding type III and IV collagen, as well as collagen cross-linking enzyme lysyl oxidase (LOX), were unchanged between groups (Fig. 3*E* and *F*). Among matrix metalloproteinases (MMPs), *Mmp2* declined, *Mmp9* did not change, and *Mmp14* increased with DIO (Fig. 3*G*). Expression of profibrotic mediator *Tgfb1* was unchanged, while that of *Tgfb3* increased in HFD-fed mice (Fig. 3*H*). Additionally, levels of *Pdgfa* and *Fgf2* were unchanged, while those of *Ctgf* and *Thbs1* increased with HFD feeding (Fig. 3*I*). These profiles suggest active and complex gene regulation underlying diaphragm ECM remodeling in long-term DIO.

Unlike DIO animals, *ob/ob* mice showed no increase in intradiaphragmatic collagen deposition versus WT controls (Supplementary Fig. 4).

FAPs Proliferate in Association With Intradiaphragmatic Adiposity and Fibrosis

We surmised that FAPs—skeletal muscle progenitors capable of differentiation into adipocytes and fibroblasts (29,30)—might underlie the fibro-adipogenic diaphragmatic remodeling observed in DIO mice. FAPs express PDGFRα and can be defined by a surface marker profile positive for Sca-1 and negative for CD31 (endothelial marker), CD45 (hematopoietic marker), and integrin α7 (satellite cell marker) (29,30). We intercrossed *PDGFRα-Cre* mice, which express Cre recombinase under the *PDGFRα* promoter, with *mT/mG* reporter mice to trace distribution of GFP$^+$ (FAP-derived) cells within the costal diaphragm (Fig. 4*A*). Significantly, GFP$^+$ cells constituted all adipocytes in 6-month CD and HFD *PDGFRα Cre-mT/mG* diaphragm samples (Fig. 4*B* and Supplementary Fig. 5*A*). These adipocytes were larger and more abundant with HFD feeding (Fig. 4*B*). We then assessed distribution of extracellular type I collagen (COL1) and type VI collagen (COL6) within costal diaphragms of the same animals. We noted expected collagen staining in epimysium and central tendon, while observing no signal in samples stained with control antibody (Supplementary Fig. 5*B–D*). CD costal diaphragms contained thin COL1 fibrils between myofiber bundles (Fig. 4*C*). COL1 bands appeared larger in HFD-fed samples, while irregular densities also surrounded clusters of GPF$^+$ stromal cells and adipocytes (Fig. 4*C*). Bands of COL6 appeared between myofibers in both groups; however, HFD diaphragms showed more prominent signal surrounding adipocyte inclusions (Fig. 4*C*).

Since PDGFRα$^+$ cells gave rise to all adipocytes and many collagen-depositing cells, we specifically analyzed

number (per mm^2 cross-sectional surface area) and measured specific (Sp) force in costal diaphragm strips subjected to isometric force testing. n = 6 CD and 7 HFD strips from animals at 6-month time point. *J*: Relative mRNA expression (Rel exp) of transcripts encoding leptin (*Lep*), fatty acid binding protein (FABP)-4 (*Ap2*), *Lpl*, adiponectin (*Adipoq*), PPARγ2 (*Pparg2*), adipsin (*Adipsin*), and TCF21 (*Tcf21*) in whole costal diaphragms of CD- and HFD-fed mice at the 6-month time point. n = 9 mice per group. *K*: mRNA level of transcript encoding UCP1 (*Ucp1*) in costal diaphragm of CD- and HFD-fed mice from the 6-month time point and in BAT from 6-month HFD-fed mice. n = 9 CD and HFD diaphragm samples and 5 BAT samples. *L*: Immunohistochemistry for UCP1 in 6-month CD and HFD costal diaphragm and 6-month HFD BAT and inguinal adipose tissue (IAT). Representative images from four animals per group. Closed arrowheads indicate UCP1-negative adipocytes, and open arrowheads indicate UCP1-positive adipocytes. Scale bar = 50 μm. Data analysis employed Student t test for two-group, single-variable comparisons, two-way ANOVA (with Sidak post hoc test) for two-variable comparisons, and linear regression for correlation testing. *$P < 0.05$; **$P < 0.01$; ***$P < 0.001$; ****$P < 0.0001$.

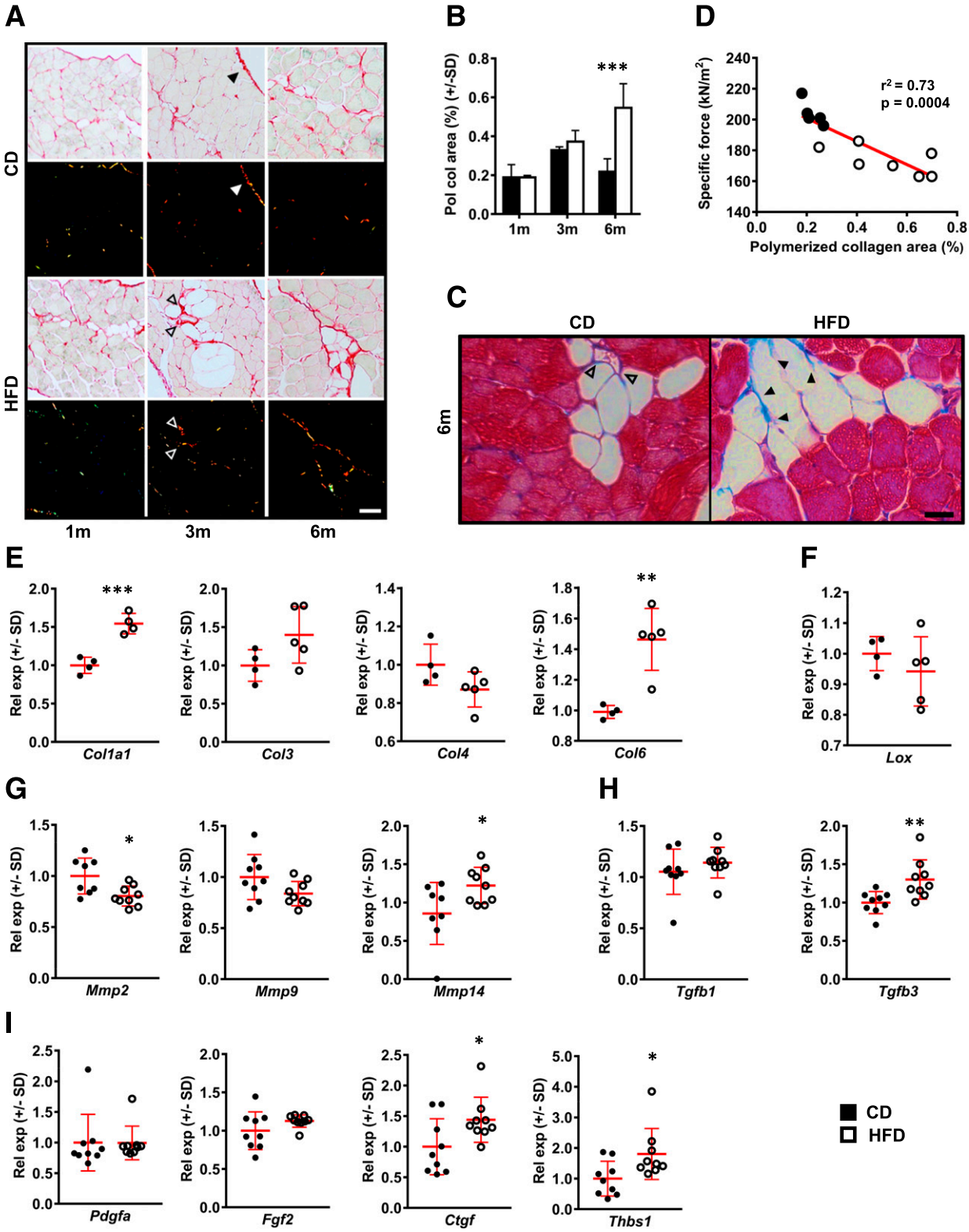

Figure 3—Progressive diaphragmatic fibrosis with DIO. *A*: Sirius red–stained costal diaphragm sections from 1-month (1m), 3-month (3m), and 6-month (6m) CD and HFD mice viewed under bright field and polarized light. Closed arrowheads indicate epimysial collagen, and open arrowheads indicate perivascular collagen—both excluded from quantitative analysis. Representative images from four animals per group at each time point. Scale bar = 50 μm. *B*: Quantification of percent total tissue surface area occupied by polymerized collagen (Pol col) detected by Sirius red staining in costal diaphragm sections of 1-month, 3-month, and 6-month CD and HFD mice. Four animals per group at each time point. *C*: Masson trichrome staining of costal diaphragm sections from 6-month CD vs. HFD mice. Demonstrates deposition of collagen (blue) around intramuscular adipocytes (closed arrowheads) more prominent in HFD-fed mice, while perivascular collagen (open arrowheads) is also prominent in CD-fed mice. Representative images from four animals per group. Scale bar = 25 μm. *D*: Correlation plot showing

response of intradiaphragmatic FAPs to HFD feeding at the 6-month time point. First, we noted increased costal diaphragm *PDGFRα* expression in HFD-fed mice (Fig. 4*D*). Next, we isolated stromal cells from costal diaphragms of *Sca-1 GFP* mice. These animals harbor an *EGFP* construct driven by *Sca-1* promoter, enabling analysis of Sca-1$^+$/CD31$^-$/CD45$^-$/integrin α7$^-$ FAPs by flow cytometry (Supplementary Fig. 6*A* and *B*). Consistent with prior reports, we found that these cells were broadly PDGFRα$^+$ (Supplementary Fig. 6*A*). In DAPI-stained stromal cell isolates, we found that both FAP number and proliferation dramatically increased with long-term obesity (Fig. 4*E*).

Obesity-Induced FAP Proliferation and Collagen Deposition

To explore the link between DIO-induced diaphragm remodeling and FAP dynamics, we analyzed gene expression profile and ex vivo fibro-adipogenic potential of these cells. Specifically, we used immunomagnetic beads to isolate stromal populations enriched for FAPs (Lin$^-$/Sca-1$^+$) and non-FAP stromal cells (Lin$^-$/Sca-1$^+$) from costal diaphragms of WT 6-month CD and HFD mice. Lin$^-$/Sca1$^+$ FAPs preferentially expressed *Pdgfra*, while Lin$^-$/Sca1$^-$ non-FAPs preferentially expressed satellite cell marker *Pax7* (Fig. 5*A*). Critically, HFD feeding induced elevated expression of *Col1*, *Col3*, and *Col6* in FAPs but not non-FAPs, implicating the former as the likely source of increased tissue-level collagens (Fig. 5*A*). Interestingly, *Tgfb3*, also globally elevated in the DIO costal diaphragm (Fig. 3*H*), increased with HFD feeding in both populations (Fig. 5*A*), suggesting that FAP-mediated fibrosis may be regulated by multiple stromal cell types.

Consistent with in vivo data, we observed greater ex vivo proliferation (Ki67 staining) in FAPs isolated from HFD-fed mice (Fig. 5*B*). COL1 deposition also increased markedly in these cells (Fig. 5*C*). Analysis of unsorted stromal cells from *PDGFRa Cre-mT/mG* mice confirmed these findings, with increased GFP$^+$ cell proliferation and collagen deposition seen in DIO costal diaphragm isolates (Supplementary Fig. 7).

In FAPs, HFD feeding induced expression of *Tcf21*, *Il6*, and *Ucp1* but not classic early adipogenesis–related genes *Pparg2*, *Cebpa*, and *Pgc1a* (Fig. 5*D*). In agreement with this, FAPs from CD- and HFD-fed mice showed equivalent ex vivo adipogenesis (Fig. 5*E*). Along with our in vivo findings, these data indicate that DIO induces FAP proliferation and collagen deposition but does not impact adipogenic potential. Increased diaphragmatic adiposity after long-term HFD feeding therefore likely results from increased FAP number.

We next sought trophic factors that might underlie FAP proliferation in the obese diaphragm. We focused on THBS1, a circulating ECM protein, produced by visceral adipose tissue (21) that acts as a potent mesenchymal cell mitogen (28). Its genetic ablation protects DIO mice from skeletal muscle fibrosis and insulin resistance (21). We first analyzed serum THBS1 level, finding it to be markedly increased in 6-month HFD mice (Fig. 5*F*). We next treated isolated FAPs with increasing THBS1 concentrations over a physiological range seen in obese humans (46). FAPs from CD-fed mice exhibited dose-dependent proliferation, whereas those from HFD-fed mice showed enhanced proliferation even at the 1 μg/mL concentration. These data highlight THBS1 as a candidate regulator of FAP proliferation and fibro-adipogenic remodeling of the DIO diaphragm.

DISCUSSION

In this study, we demonstrated that the mouse diaphragm undergoes progressive fibro-adipogenic remodeling with long-term HFD-feeding, ultimately exhibiting impaired motion in vivo and contraction ex vivo. The temporal correlation between fibro-adipogenic changes and diaphragm dysfunction, coupled with identification of proliferating FAPs as a likely remodeling driver, provides a framework for better understanding respiratory impairment in obesity.

Our data demonstrate that DIO of considerable duration is needed to cause respiratory compromise in mice. Noninvasive US found no significant diaphragm motion changes after 3 months of HFD feeding but revealed shallow, short-interval breaths with increased duty cycle by 6 months. This approximates breathing patterns of obese humans (1,5). As previously shown in *mdx* mice (a muscular dystrophy model with primary diaphragm dysfunction) (36), low excursion amplitudes seen on US correlated with reduced specific force measured ex vivo. In turn, specific force correlated negatively with body weight and adiposity measures. This parallels the increasing risk of obesity-associated respiratory dysfunction clinically observed at higher BMI (2). Elevated intradiaphragmatic adipocyte number and polymerized collagen content emerged only at the 6-month time point, when

relationship between polymerized collagen area (percent cross-sectional surface area occupied by birefringence) and measured specific force in costal diaphragm strips subjected to isometric force testing. n = 6 CD and 7 HFD strips from animals at 6-month time point. *E–I*: Relative mRNA expression (Rel exp) of transcripts encoding collagen species, collagen-processing proteins, and mediators of tissue fibrosis in whole costal diaphragms of 6-month CD and HFD mice. n = 5–9 animals per group: type I collagen (*Col1a1*), type III collagen (*Col3*), type IV collagen (*Col4*), and type VI collagen (*Col6*) (*E*); *Lox* (*F*); MMP2 (*Mmp2*), MMP-9 (*Mmp9*), and MMP-14 (*Mmp14*) (*G*); TGF-β1 (*Tgfb1*) and TGF-β3 (Tgfb3) (*H*); and PDGF-AA (*Pdgfa*), fibroblast growth factor (FGF)2 (*Fgf2*), connective tissue growth factor (CTGF) (*Ctgf*), and thrombospondin (TSP)-1 (Thbs1) (*I*). Data analysis employed Student t test for two-group, single-variable comparisons; two-way ANOVA (with Sidak post hoc test) for two-variable comparisons; and linear regression for correlation testing. $^*P < 0.05$; $^{**}P < 0.01$; $^{***}P < 0.001$.

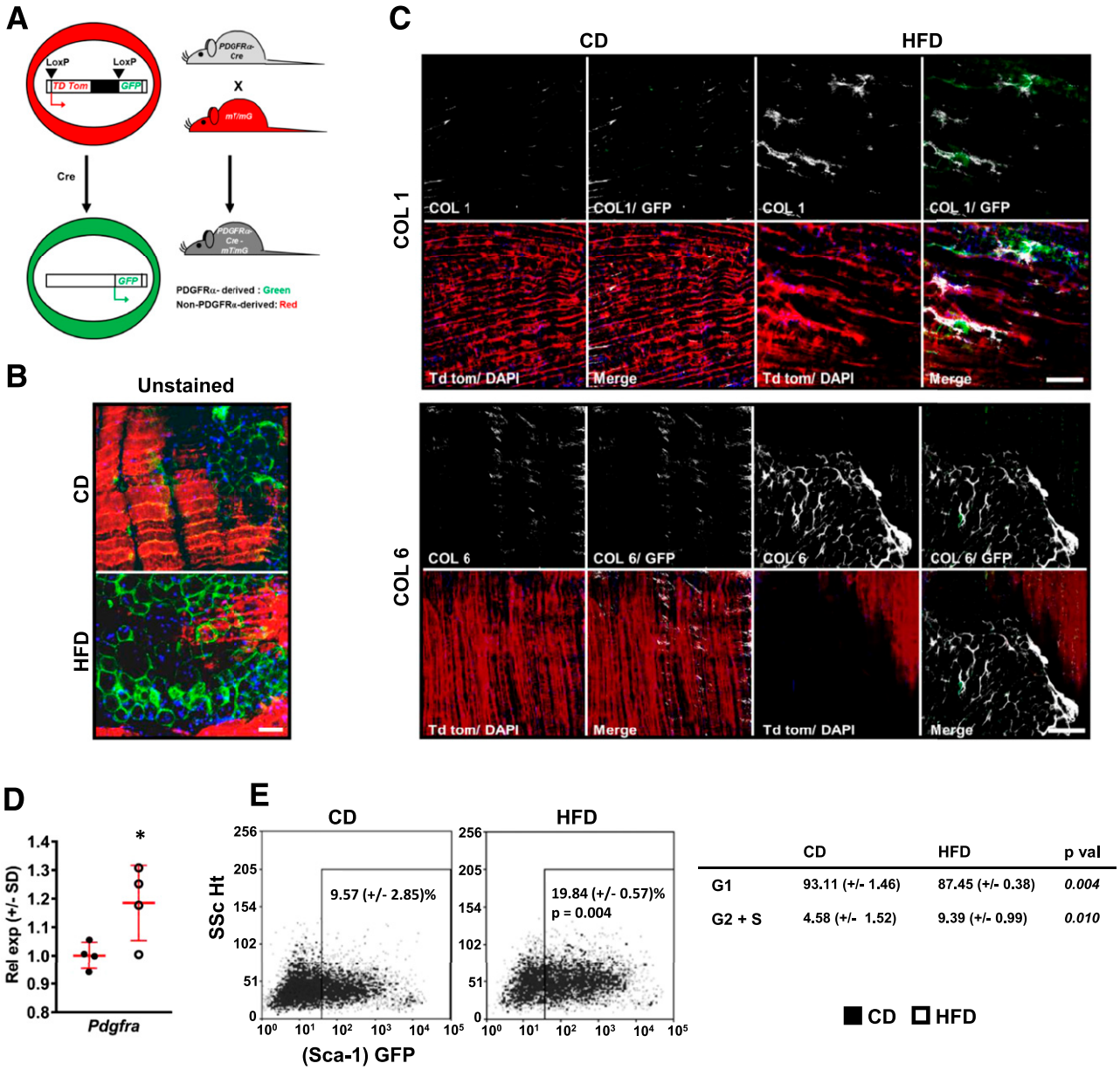

	CD	HFD	p val
G1	93.11 (+/- 1.46)	87.45 (+/- 0.38)	*0.004*
G2 + S	4.58 (+/- 1.52)	9.39 (+/- 0.99)	*0.010*

Figure 4—Diaphragm FAPs give rise to adipocytes and collagen-producing cells in DIO mice. *A*: *PDGFRα Cre-mT/mG* mouse model used for lineage tracing of cells derived from PDGFRα$^+$ precursors as GFP$^+$ cells and others as Td tomato (Td tom)$^+$ cells. *B*: Confocal whole-mount images of unstained diaphragms from 6-month CD and HFD *PDGFRα Cre-mT/mG* mice. Representative images from four animals per group. Scale bar = 50 μm. *C*: Immunostaining for COL1 and COL6, respectively, in whole-mount costal diaphragm samples from the same animals. Note deposition of COL1 near GFP$^+$ cells and distribution of COL6 surrounding clusters of adipocytes. Scale bar = 100 μm. *D*: *Pdgfra* mRNA levels in whole costal diaphragms of WT C57Bl/6 mice fed CD or HFD for 6 months. *n* = 4 CD-fed and 5 HFD-fed animals. *E*: Flow cytometry plots showing percent GFP$^+$/CD31$^-$/CD45$^-$/integrin α7$^-$ nucleated cells (FAPs) among total nucleated cells isolated from costal diaphragms of 6-month CD and HFD *Sca-1 GFP* mice. Representative plots (each showing cells from the costal diaphragm of a single animal) from four unique experiments. Table shows percentage of FAPs in G1 and G2 + S phase (analyzed using DAPI signals). Data analysis employed Student *t* test. p val, *P* value. Rel exp, relative expression between groups; SSc Ht, side scatter height. *$P < 0.05$.

diaphragm dysfunction manifested, and correlated quantitatively with specific force decrements.

Equally obese but relatively young (16-week-old) leptin-deficient *ob/ob* mice showed similar diaphragm motion defects, with lower amplitude, inspiratory velocity, and expiratory velocity; however, they had nearly identical duty cycle and ex vivo specific force versus age-matched controls. *Ob/ob* diaphragms also did not demonstrate increased adipocyte number or polymerized collagen as seen with long-term DIO. These findings suggest that hypoventilation in *ob/ob* mice occurs independent of primary diaphragm compromise. Indeed, leptin is a key regulator of central respiratory control (47), and its administration reverses ventilatory defects observed in *ob/ob* but not

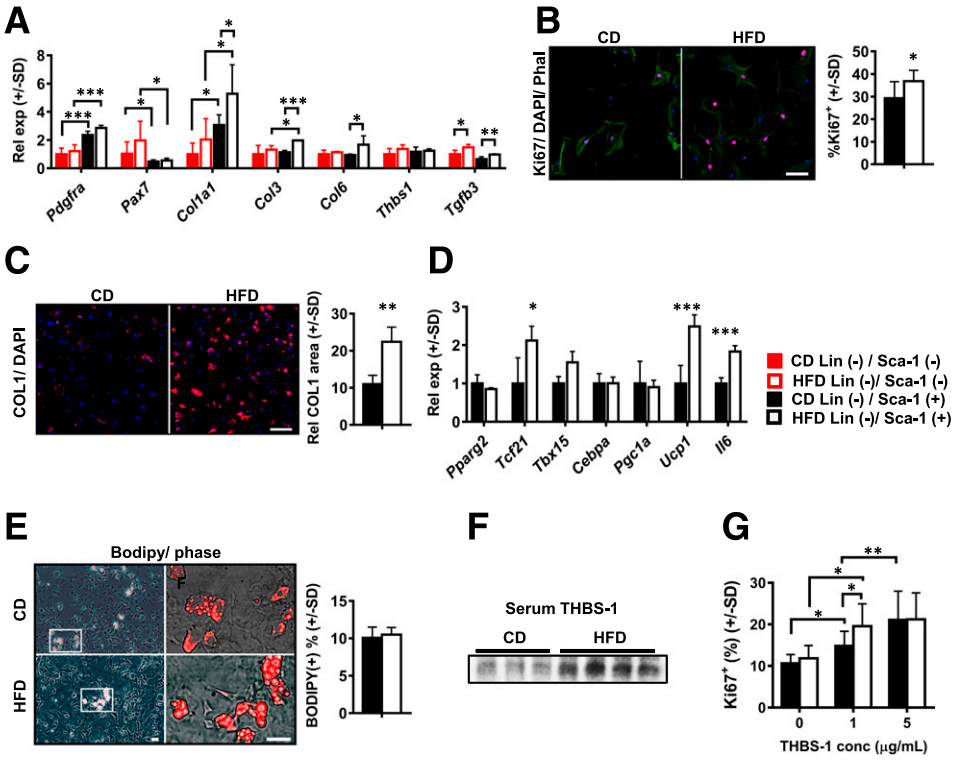

Figure 5—Isolated FAPs demonstrate obesity-induced fibrotic gene expression signature, with increased ex vivo proliferation and collagen deposition. *A*: Relative mRNA levels in Lin$^-$ (CD31 and CD45)/Sca1$^+$ stromal cells (FAPs) and Lin$^-$/Sca-1$^-$ stromal cells (non-FAPs) isolated from costal diaphragms of mice fed CD or HFD for 6 months. Each sample consists of pooled stromal isolate from three CD- or two HFD-fed animals. Each group contains four samples. Transcripts analyzed are those encoding PDGFRα (*Pdgfra*), Pax7 (*Pax7*), type I collagen (*Col1a1*), type III collagen (*Col3*), *Col6*, THBS1 (*Thbs1*), and TGF-β3 (*Tgfb3*). *B*: Ki67 staining (red) of isolated FAPs from mice fed CD or HFD for 6 months cultured in standard medium with 10% FBS. Phalloidin counterstain (Phal, green) and DAPI nuclear stain (blue) were used. Representative images of three unique experiments, each comparing three CD- and two HFD-fed mice. Scale bar = 25 μm. Bar graph indicates quantification of Ki67$^+$ nuclei/total nuclei in ten 10× fields per group in each experiment. *C*: Type I collagen immunocytochemistry in FAPs isolated from 6-month CD and HFD mice and cultured in standard medium with 10% FBS. Representative images of three unique experiments, each including three CD- and two HFD-fed mice. Quantification of relative (Rel) surface area occupied by COL1 in ten 10× fields per group in each experiment (normalized to cell number). Scale bar = 50 μm. *D*: Gene expression profiling in Lin$^-$/Sca1$^+$ FAPs from 6-month CD and HFD mice. Transcripts analyzed include those encoding PPARγ2 (*Pparg2*), TCF21 (*Tcf21*), T-box (TBX)15 (*Tbx15*), CEBPα (*Cepba*), PGC1a (*Pgc1a*), UCP1 (*Ucp1*), and IL6 (*Il6*). *E*: BODIPY staining in FAPs isolated from 6-month CD and HFD mice and subjected to adipogenic differentiation protocol. Representative images of three unique experiments, each including three CD- and two HFD-fed mice. Quantification of ten 10× fields per group per experiment. Scale bar = 25 μm. *F*: Western blot for THBS1 in plasma of 6-month CD and HFD mice. $n = 3$ CD-fed and 4 HFD-fed mice. *G*: Proliferation of FAPs isolated from 6-month CD and HFD mice cultured in medium containing 1% FBS supplemented with concentration (conc) of 0, 1, or 5 μg/mL THBS1. Proliferation calculation based on percentage of Ki67$^+$ nuclei/total nuclei in ten 10× fields per group per experiment. Based on three unique experiments, each including three CD- and two HFD-fed mice. Data analysis employed Student *t* test for two-group comparisons, one-way ANOVA (with Tukey post hoc test) for comparison of two or more groups, and two-way ANOVA (with Sidak post hoc test) for two variables. Rel exp, relative expression between groups. $^*P < 0.05$; $^{**}P < 0.01$; $^{***}P < 0.001$.

DIO mice (12). We therefore surmise that chronicity of HFD feeding, with potential contribution from dietary content, underlies diaphragm anatomic remodeling and contractile dysfunction not seen in the younger *ob/ob* mice. The premise that long-term obesity is needed to induce intrinsic diaphragm defects may explain discrepancies in previous analyses of *ZDF* rats. In that model, while diaphragm isolates from young animals (3–4 months old) demonstrate unchanged or even increased (9–11) isometric force, those from older animals (8 months old) show force reduction (8).

IMAT accumulation and tissue fibrosis are both associated with skeletal muscle contractile dysfunction (16–20) and occur in obesity (17–19,21–26). In our DIO model, FAPs emerged as likely drivers of diaphragm fibro-adipogenic remodeling, giving rise to all adipocytes and many collagen-producing fibroblast-like cells. HFD feeding caused FAPs to proliferate and assume a fibrogenic phenotype. Since FAPs from HFD-fed mice had similar adipogenic potential versus controls, we reason that adipocyte accumulation in long-term DIO results from slow but progressive adipocyte differentiation from a larger FAP pool. FAPs from HFD-fed mice were nonetheless qualitatively different, exhibiting elevated expression of specific adipocyte-related genes. *Tcf21*, a WAT marker (42), recently shown to be enriched in visceral adipose stem cells (38), was induced in FAPs with HFD feeding, as was *Il6*, a TCF21-regulated gene (38). HFD feeding also upregulated FAP-specific expression of *Ucp1*, corresponding with presence of scattered UCP1$^+$ unilocular

adipocytes in DIO diaphragms. Interestingly, *Ucp1* upregulation in FAPs and the presence of adipocytes positive for UCP-1 were demonstrated in mouse tibialis anterior muscles subjected to toxin-induced injury (48). Specific contributions of increased intramuscular adiposity and fibrosis to contractile dysfunction remain elusive but represent tractable areas of inquiry with improved understanding of FAP dynamics in obesity.

Our identification of THBS1—a WAT-derived, circulating ECM protein increased in obesity and type 2 diabetes (46)—as a mediator of FAP proliferation provides one link between overnutrition and diaphragm fibro-adipogenic remodeling. Recent work has identified THBS1 as a stromal cell mitogen, acting in concert with known FAP growth factors TGF-β and PDGF-AA (28). Since THBS1 also regulates skeletal muscle fibrosis (21), further evaluating its impact on FAPs will enable novel mechanistic exploration of diaphragm structure/function compromise in obesity.

Funding. Research reported here was supported by the National Institute of Arthritis and Musculoskeletal and Skin Diseases (NIAMS) of the National Institutes of Health (NIH) under award P30AR069620, National Institute of Diabetes and Digestive and Kidney Diseases (NIDDK) grant R01-DK-095137 (to T.-H.C.), and the University of Michigan Biomedical Research Council Fund (to T.-H.C.). E.D.B. is supported by the Marilyn Fishman Grant for Endocrinology Research from the Endocrine Fellows Foundation and NIDDK T32-DK-007696. D.E.M. is partially supported by NIAMS R01AR068428. The University of Michigan Animal Phenotyping Core, in which ultrasound experiments were performed, also receives support for training from NIH Office of the Director K26OD016502 to D.E.M.

The content of this publication is solely the responsibility of the authors and does not necessarily represent the official views of the National Institutes of Health.

Duality of Interest. No potential conflicts of interest relevant to this article were reported.

Author Contributions. E.D.B., K.C.-B., C.S.D., and T.A. performed the experiments. E.D.B., D.E.M., S.V.B., and T.-H.C. evaluated data. E.D.B. and T.-H.C. conceived of the research idea and designed experiments. E.D.B. and T.-H.C. wrote the manuscript. E.D.B., K.C.-B., C.S.D., T.A., F.H., D.E.M., S.V.B., and T.-H.C. reviewed the manuscript. T.A., F.H., D.E.M., and S.V.B. provided technical consultation. T.-H.C. is the guarantor of this work and, as such, had full access to all the data in the study and takes responsibility for the integrity of the data and the accuracy of the data analysis.

References

1. De Jong A, Chanques G, Jaber S. Mechanical ventilation in obese ICU patients: from intubation to extubation. Crit Care 2017;21:63

2. Balachandran JS, Masa JF, Mokhlesi B. Obesity hypoventilation syndrome epidemiology and diagnosis. Sleep Med Clin 2014;9:341–347

3. Castro-Añón O, Pérez de Llano LA, De la Fuente Sánchez S, et al. Obesity-hypoventilation syndrome: increased risk of death over sleep apnea syndrome. PLoS One 2015;10:e0117808

4. Pierce AM, Brown LK. Obesity hypoventilation syndrome: current theories of pathogenesis. Curr Opin Pulm Med 2015;21:557–562

5. Chlif M, Keochkerian D, Choquet D, Vaidie A, Ahmaidi S. Effects of obesity on breathing pattern, ventilatory neural drive and mechanics. Respir Physiol Neurobiol 2009;168:198–202

6. Lin CK, Lin CC. Work of breathing and respiratory drive in obesity. Respirology 2012;17:402–411

7. Fadell EJ, Richman AD, Ward WW, Hendon JR. Fatty infiltration of respiratory muscles in the Pick-wickian syndrome. N Engl J Med 1962;266:861–863

8. Farkas GA, Gosselin LE, Zhan WZ, Schlenker EH, Sieck GC. Histochemical and mechanical properties of diaphragm muscle in morbidly obese Zucker rats. J Appl Physiol (1985) 1994;77:2250–2259

9. van Lunteren E. Effects of genetic obesity on rat upper airway muscle and diaphragm contractile properties. Eur Respir J 1996;9:2139–2144

10. Allwood MA, Foster AJ, Arkell AM, et al. Respiratory muscle weakness in the Zucker diabetic fatty rat. Am J Physiol Regul Integr Comp Physiol 2015;309: R780–R787

11. De Jong A, Carreira S, Na N, et al. Diaphragmatic function is enhanced in fatty and diabetic fatty rats. PLoS One 2017;12:e0174043

12. O'donnell CP, Schaub CD, Haines AS, et al. Leptin prevents respiratory depression in obesity. Am J Respir Crit Care Med 1999;159:1477–1484

13. Manini TM, Clark BC, Nalls MA, Goodpaster BH, Ploutz-Snyder LL, Harris TB. Reduced physical activity increases intermuscular adipose tissue in healthy young adults. Am J Clin Nutr 2007;85:377–384

14. Torriani M, Townsend E, Thomas BJ, Bredella MA, Ghomi RH, Tseng BS. Lower leg muscle involvement in Duchenne muscular dystrophy: an MR imaging and spectroscopy study. Skeletal Radiol 2012;41:437–445

15. Delmonico MJ, Harris TB, Visser M, et al.; Health, Aging, and Body. Longitudinal study of muscle strength, quality, and adipose tissue infiltration. Am J Clin Nutr 2009;90:1579–1585

16. Goodpaster BH, Chomentowski P, Ward BK, et al. Effects of physical activity on strength and skeletal muscle fat infiltration in older adults: a randomized controlled trial. J Appl Physiol (1985) 2008;105:1498–1503

17. Hilton TN, Tuttle LJ, Bohnert KL, Mueller MJ, Sinacore DR. Excessive adipose tissue infiltration in skeletal muscle in individuals with obesity, diabetes mellitus, and peripheral neuropathy: association with performance and function. Phys Ther 2008;88:1336–1344

18. Bittel DC, Bittel AJ, Tuttle LJ, et al. Adipose tissue content, muscle performance and physical function in obese adults with type 2 diabetes mellitus and peripheral neuropathy. J Diabetes Complications 2015;29:250–257

19. Almurdhi MM, Reeves ND, Bowling FL, Boulton AJ, Jeziorska M, Malik RA. Reduced lower-limb muscle strength and volume in patients with type 2 diabetes in relation to neuropathy, intramuscular fat, and vitamin D levels. Diabetes Care 2016;39:441–447

20. Chapman MA, Meza R, Lieber RL. Skeletal muscle fibroblasts in health and disease. Differentiation 2016;92:108–115

21. Inoue M, Jiang Y, Barnes RH II, et al. Thrombospondin 1 mediates high-fat diet-induced muscle fibrosis and insulin resistance in male mice. Endocrinology 2013;154:4548–4559

22. Kang L, Ayala JE, Lee-Young RS, et al. Diet-induced muscle insulin resistance is associated with extracellular matrix remodeling and interaction with integrin alpha2beta1 in mice. Diabetes 2011;60:416–426

23. Kang L, Mayes WH, James FD, Bracy DP, Wasserman DH. Matrix metalloproteinase 9 opposes diet-induced muscle insulin resistance in mice. Diabetologia 2014;57:603–613

24. Richardson DK, Kashyap S, Bajaj M, et al. Lipid infusion decreases the expression of nuclear encoded mitochondrial genes and increases the expression of extracellular matrix genes in human skeletal muscle. J Biol Chem 2005;280: 10290–10297

25. Tam CS, Covington JD, Bajpeyi S, et al. Weight gain reveals dramatic increases in skeletal muscle extracellular matrix remodeling. J Clin Endocrinol Metab 2014;99:1749–1757

26. Berria R, Wang L, Richardson DK, et al. Increased collagen content in insulin-resistant skeletal muscle. Am J Physiol Endocrinol Metab 2006;290:E560–E565

27. Crawford SE, Stellmach V, Murphy-Ullrich JE, et al. Thrombospondin-1 is a major activator of TGF-β1 in vivo. Cell 1998;93:1159–1170

28. Belotti D, Capelli C, Resovi A, Introna M, Taraboletti G. Thrombospondin-1 promotes mesenchymal stromal cell functions via TGFβ and in cooperation with PDGF. Matrix Biol 2016;55:106–116

29. Joe AW, Yi L, Natarajan A, et al. Muscle injury activates resident fibro/adipogenic progenitors that facilitate myogenesis. Nat Cell Biol 2010;12:153–163

30. Uezumi A, Fukada S, Yamamoto N, Takeda S, Tsuchida K. Mesenchymal progenitors distinct from satellite cells contribute to ectopic fat cell formation in skeletal muscle. Nat Cell Biol 2010;12:143–152
31. Uezumi A, Fukada S, Yamamoto N, et al. Identification and characterization of PDGFRα+ mesenchymal progenitors in human skeletal muscle. Cell Death Dis 2014;5:e1186
32. Heredia JE, Mukundan L, Chen FM, et al. Type 2 innate signals stimulate fibro/adipogenic progenitors to facilitate muscle regeneration. Cell 2013;153:376–388
33. Lemos DR, Babaeijandaghi F, Low M, et al. Nilotinib reduces muscle fibrosis in chronic muscle injury by promoting TNF-mediated apoptosis of fibro/adipogenic progenitors. Nat Med 2015;21:786–794
34. Uezumi A, Ito T, Morikawa D, et al. Fibrosis and adipogenesis originate from a common mesenchymal progenitor in skeletal muscle. J Cell Sci 2011;124:3654–3664
35. Mozzetta C, Consalvi S, Saccone V, et al. Fibroadipogenic progenitors mediate the ability of HDAC inhibitors to promote regeneration in dystrophic muscles of young, but not old Mdx mice. EMBO Mol Med 2013;5:626–639
36. Whitehead NP, Bible KL, Kim MJ, Odom GL, Adams ME, Froehner SC. Validation of ultrasonography for non-invasive assessment of diaphragm function in muscular dystrophy. J Physiol 2016;594:7215–7227
37. Brooks SV, Faulkner JA. Contractile properties of skeletal muscles from young, adult and aged mice. J Physiol 1988;404:71–82
38. Akama T, Chun T-H. Transcription factor 21 (TCF21) promotes proinflammatory interleukin 6 expression and extracellular matrix remodeling in visceral adipose stem cells. J Biol Chem 2018;293:6603–6610
39. Biltz NK, Meyer GA. A novel method for the quantification of fatty infiltration in skeletal muscle. Skelet Muscle 2017;7:1
40. Stuelsatz P, Keire P, Almuly R, Yablonka-Reuveni Z. A contemporary atlas of the mouse diaphragm: myogenicity, vascularity, and the Pax3 connection. J Histochem Cytochem 2012;60:638–657
41. Pickering M, Jones JF. The diaphragm: two physiological muscles in one. J Anat 2002;201:305–312
42. de Jong JM, Larsson O, Cannon B, Nedergaard J. A stringent validation of mouse adipose tissue identity markers. Am J Physiol Endocrinol Metab 2015;308:E1085–E1105
43. Flier JS, Cook KS, Usher P, Spiegelman BM. Severely impaired adipsin expression in genetic and acquired obesity. Science 1987;237:405–408
44. Lumeng CN, Bodzin JL, Saltiel AR. Obesity induces a phenotypic switch in adipose tissue macrophage polarization. J Clin Invest 2007;117:175–184
45. Almind K, Manieri M, Sivitz WI, Cinti S, Kahn CR. Ectopic brown adipose tissue in muscle provides a mechanism for differences in risk of metabolic syndrome in mice. Proc Natl Acad Sci U S A 2007;104:2366–2371
46. Matsuo Y, Tanaka M, Yamakage H, et al. Thrombospondin 1 as a novel biological marker of obesity and metabolic syndrome. Metabolism 2015;64:1490–1499
47. Bassi M, Furuya WI, Zoccal DB, et al. Facilitation of breathing by leptin effects in the central nervous system. J Physiol 2016;594:1617–1625
48. Gorski T, Mathes S, Krützfeldt J. Uncoupling protein 1 expression in adipocytes derived from skeletal muscle fibro/adipogenic progenitors is under genetic and hormonal control. J Cachexia Sarcopenia Muscle 2018;9:384–399